

PROCEEDINGS OF SPIE

[SPIDigitalLibrary.org/conference-proceedings-of-spie](https://spiedigitallibrary.org/conference-proceedings-of-spie)

A dual-wavelength spread spectrum-based spectroscopic system For time-domain near-infrared diffuse optical imaging

Konstantinos I. Papadimitriou, Jeremy C. Hebden, Simon R. Arridge, Samuel Powell

Konstantinos I. Papadimitriou, Jeremy C. Hebden, Simon R. Arridge, Samuel Powell, "A dual-wavelength spread spectrum-based spectroscopic system For time-domain near-infrared diffuse optical imaging," Proc. SPIE 10874, Optical Tomography and Spectroscopy of Tissue XIII, 1087421 (1 March 2019); doi: 10.1117/12.2507992

SPIE.

Event: SPIE BiOS, 2019, San Francisco, California, United States

A Dual-Wavelength Spread Spectrum-Based Spectroscopic System For Time-Domain Near-Infrared Diffuse Optical Imaging

Konstantinos I. Papadimitriou^a, Jeremy C. Hebden^b, Simon R. Arridge^a, and Samuel Powell^c

^aDepartment of Computer Science, ^bDepartment of Medical Physics & Biomedical Engineering, University College London, WC1E 6BT, London, UK

^c Biomedical Engineering & Imaging Sciences, King's College London, SE1 7EU, London, UK

ABSTRACT

We advance our previous research on spread spectrum spectroscopy by adding spectroscopic functionality using a custom-made optical transceiver. The new transceiver module features a 680nm communications-grade vertical-cavity surface-emitting laser (VCSEL) and matches the performance of commercial 10Gb/s optical transceivers, which allow for a sub-ns instrument response. The optical power of the VCSEL can be software-adjusted up to 2mW with $\sim 40\mu\text{A}$ driving current resolution. This module, combined with a commercially available Gigabit optical transceiver at 850nm, allows us to derive information about the optical properties of tissue-equivalent phantoms and the concentration of various haemodynamic parameters in *in vivo* measurements.

Keywords: field programmable gate array, near infrared spectroscopy, optical transceiver, spread spectrum, time-domain, vertical-cavity surface-emitting laser

1. INTRODUCTION

Near-infrared spectroscopy (NIRS) is a non-invasive monitoring modality that allows for real-time measurements of oxygenated haemoglobin (HbO_2), de-oxygenated haemoglobin (HHb), total haemoglobin (tHb) and oxygen saturation (SO_2) level changes in tissues. This optical technique can also record sensitive, real-time brain haemodynamics while the subject is performing a functional task¹. In the latter case the technique is called functional NIRS (fNIRS), which once combined with multiple sources and detectors on the subject under test, it can reconstruct three-dimensional images of changes in the optical properties of that target object². This multi source-detector imaging technique is called diffuse optical tomography (DOT) and provides significant spatial information that can map the human brain non-invasively and in real time^{3,4}.

Despite the large variety of NIRS systems, the vast majority of them revolve around three main categories: (i) continuous wave (CW); (ii) frequency domain (FD) and (iii) time domain (TD). Through the CW modality, the light attenuation of a constantly illuminated tissue is recorded, while in FD the sample is illuminated with intensity-modulated light and both attenuation and phase delay of emerging light is measured. On the other hand, with the TD method an ultra-short light pulse (circa few picoseconds pulse width) from the source is injected into the turbid medium and the photon distribution of the time-of-flight (DToF) is measured at the detector^{1,4}. Although CW instruments are the most commercially exploited to date, in part owing to their simplicity and cost-effectiveness, the facility of TD NIRS to measure photon pathlengths in biological tissue enables more accurate recovery of absolute optical properties and greater depth sensitivity when used in DOT applications. However, TD NIRS systems, in contrast to CW instruments, are typically bulky and expensive, and employ sensitive optoelectronics that often inhibit translation of the technique beyond the research environment. Spread spectrum methods are being investigated in an attempt to overcome some of the challenges involved in using conventional pulsed laser sources and time-of-flight (ToF) technology⁵⁻⁸. Herein, we demonstrate characterisation and preliminary *in vivo* results of the first dual-wavelength instrument in literature that exploits a spread spectrum approach for TD NIRS measurements.

Further author information: (Send correspondence to K.I.P)
K.I.P.: E-mail: k.papadimitriou@ucl.ac.uk

2. EXCITATION METHOD & SYSTEM DESCRIPTION

As discussed above, TD instruments record the time required for single photons to travel through samples/tissues, once an ultra-short pulse is injected from the source into the turbid medium. With the use of very fast detectors, based on a technique called time correlated single photon counting (TCSPC), a histogram of the time each photon required to travel from source to the detector is formed. This histogram is also known as temporal point spread function (TPSF) and reveals how much the original pulse has broadened and attenuated⁹, offering useful absolute optical properties and depth information of the subject under test. In traditional pulse excitation (PE)-based TD NIRS instruments for TCSPC, the following linear relationship holds between the measured TPSF and the real TPSF:

$$\text{TPSF}_{\text{Meas.}}^{\text{PE}}(t) = \text{IRF}^{\text{PE}}(t) * \text{TPSF}_{\text{Real}}(t), \quad (1)$$

where $*$ denotes convolution. In this case, for the system's impulse response function ($\text{IRF}^{\text{PE}}(t)$) it holds that:

$$\text{IRF}^{\text{PE}}(t) = \text{Laser Pulse}(t) * \text{Source IRF}(t) * \text{Detector IRF}(t), \quad (2)$$

with the source and detector IRFs depending on the properties of the selected optical fibres and the coupling between different optical components in the setup and also between the optics and the subject under test^{8,9}.

2.1 THE SPREAD SPECTRUM PARADIGM

Spread spectrum methods have been widely used in telecommunications due to the low bit-error rate, interference rejection and selective addressing capabilities that they exhibit¹⁰. The core idea behind spread spectrum techniques is that a signal of specific bandwidth can be *spread* in the frequency domain, resulting into a lower instantaneous power signal which makes use of the full bandwidth of the communication channel. This idea has been successfully applied to TD NIRS as an alternative to pulsed excitation⁵⁻⁸, aiming at overcoming some of the aforementioned instrumental challenges of traditional TD systems. Following a spread spectrum-based approach in TD NIRS would allow us to use lower power sources for tissue excitation, such as VCSELs, which are significantly cheaper compared to traditional pulsed excitation lasers, and can be modulated constantly at very high speed rates.

In telecommunications, a pseudorandom binary sequence (PRBS) is usually employed in order to spread a modulated signal over a bandwidth, much greater than the bandwidth of the signal itself. In the spread spectrum content, the PRBS is also called pseudo noise (PN), since its spectrum approaches that of random noise. In our time-resolved system, the input signal that is mixed with the PRBS is the system's IRF, thus, the response recorded by the TCSPC card ($G^{\text{SS}}(t)$) does not resemble a conventional distribution of the ToF. The recorded TCSPC histogram is the convolution of the transmitted PRBS with the system's IRF and the impulse response of the medium:

$$G^{\text{SS}}(t) = \text{IRF}^{\text{SS}}(t) * P(t) * \text{TPSF}_{\text{Real}}(t), \quad (3)$$

with $P(t)$ denoting the binary sequence with which the VCSEL is modulated⁸. In this work, a maximum-length sequences (MLS) has been chosen again to be optically transmitted by our spectroscopic system, due to its excellent, delta function-like, autocorrelation properties. By cross-correlating the obtained ToF photon distribution, $G^{\text{SS}}(t)$, with the binary transmitted MLS, $P(t)$, which modulates the system's VCSELs, the following relationship holds for the measured TPSF:

$$\text{TPSF}^{\text{SS}}(\tau) = \langle G^{\text{SS}}(t)P^*(t - \tau) \rangle = \text{IRF}^{\text{SS}}(\tau) * R_{XX}(\tau) * \text{TPSF}_{\text{Real}}(\tau), \quad (4)$$

with $\text{TPSF}^{\text{SS}}(\tau)$ representing the measured TPSF of the subject under test, valid only when the TPSF's duration is less than the transmitted MLS period and $R_{XX}(\tau)$ denoting the autocorrelation function of the transmitted MLS⁸.

2.2 SYSTEM CONFIGURATION

A schematic representation of the implemented dual-wavelength spread spectrum-based TD instrument can be found in Figure 1. The system's architecture is similar to the single-wavelength spread spectrum setup, originally proposed in our previous work⁸. However, in the current setup appropriate changes and additions have been made, in order to facilitate the spectroscopic functionality of the instrument. More specifically, a custom-made optical transceiver has been added, featuring a 680nm communications-grade VCSEL (680C-0000-B002, VIXAR Inc.). The optical transceiver has been fabricated on a custom-made 4-layer, 1mm thickness printed circuit board (PCB) with dimensions 12×63mm. One end of the PCB has been designed to mate directly with the standard 20-contacts industrial SFP/SFP+ electrical connectors, incorporating the required power, ground and signal pads. A low-power integrated limiting amplifier and VCSEL driver Integrated Circuit (IC)(MAX3798, Maxim) has been used to drive the 680nm VCSEL at 10Gb/s by providing appropriate modulation and bias currents, both fully controllable via a 3-wire interface. The VCSEL driver can provide modulation current up to 12mA and bias current up to 15mA, with deterministic jitter <6ps and rise and fall times at the transmitter output down to 26ps. The high-speed PCB tracks have been designed carefully using impedance control techniques, taking into consideration the required differential input resistance of the VCSEL driver and the resistance of the VCSEL. Finally, the 680nm VCSEL TO-can package has been reinforced with a compact ~8×16mm radiator for better heat dissipation.

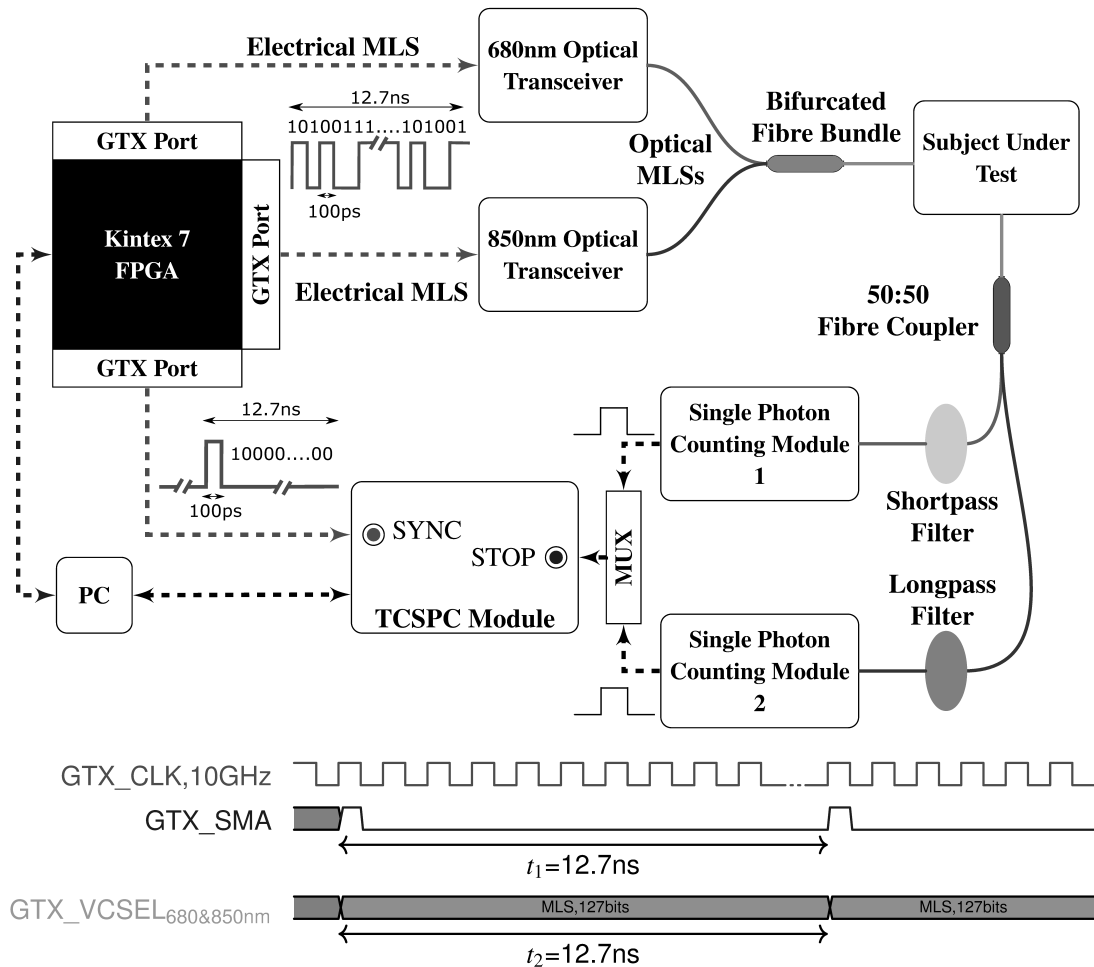


Figure 1. A schematic diagram of the dual-wavelength spread spectrum-based TD system. The timing diagram at the bottom of the Figure demonstrates the synchronous transmission of all FPGA's GTX transmitter ports.

The 680nm custom-made optical transceiver described above combined with the commercially available Gigabit optical transceiver (AFBR-709SMZ, Avago), utilising an 850nm VCSEL⁸, provide the required two wavelengths to our spectroscopic TD system. Once again, the two VCSELs are modulated at 10Gb/s by the Multi-Gigabit Transceivers (MGTs) of a Kintex 7 FPGA (KC705, Xilinx), called *GTX Transceivers*. This time three GTX ports of Kintex 7 FPGA have been employed, all programmed to operate at 10Gb/s in a synchronous manner, clocked by the same, dedicated GTX reference clock. The two GTX ports modulating the two optical transceivers are transmitting the same fixed length MLS electrical signal, which after the optical transmitters is converted into an optical MLS signal. An MLS with length $N_{MLS}=2^q-1$ and $q=7$ has been chosen again, corresponding to a sequence with 12.7ns period. This period is sufficiently long so that the recorded TPSFs are fully expressed and not *clipped*. The third GTX port is again transmitting a single 100ps width electrical pulse with the same period as the MLS. This signal is used as the **SYNC** signal of the TCSPC card (SPC-130, Becker & Hickl). Because the KC705 has only one dedicated SFP+ port, a quad SFP/SFP+ transceiver FMC (VITA 57) module (Faster Technology) has been used for the connection of the second optical transceiver to the FPGA board.

The optical MLS outputs of the two transceivers are connected to a 50/125 μ m (core/cladding), 2 \times 1, SMA905 fibre bundle (BFY50LS02, Thorlabs), which is subsequently coupled to the subjects under test. On the detector side, a 50/125 μ m, 1 \times 2, 50:50 fibre coupler (TM50R5F1A, Thorlabs) has been employed to collect the diffused two-wavelength light and splits it into two symmetrical *free-space* branches. Each branch collimates the light coming out of the fibre coupler, filters the appropriate wavelength using a shortpass or a longpass filter, respectively, and finally couples the resulting single wavelength light into a 50/125 μ m multi-mode fibre (M42L01, Thorlabs), which is subsequently directly coupled to a single photon counting module (SPCM). Light collimation and coupling is achieved using a combination of appropriate plano-convex lenses. Both SPCMs used in this setup feature a thermoelectrically cooled and temperature controlled silicon avalanche photodiode (SPCM-AQR-14-FC & SPCM-AQRH-14-FC, PerkinElmer) and have similar timing characteristics. The TTL signals from the SPCMs' outputs act as the **EVENT** electrical signals for the TCSPC acquisition card. Because the SPC-130 is a single channel TCSPC card, an 8-channel router has been employed (HRT-81, Becker & Hickl) to accommodate both high-speed **EVENT** signals, without affecting their integrity. The collected data have been post-processed in a manner, identical to the one originally shown in our previous related work⁸.

3. SYSTEM CHARACTERISATION

The instrument has been characterised based on a set of standardised experiments for TD NIRS systems, as already shown before⁸. More specifically, the system's IRFs' full width half maximum (FWHM) have been computed, together with the long-term stability, linearity and accuracy of each VCSEL source.

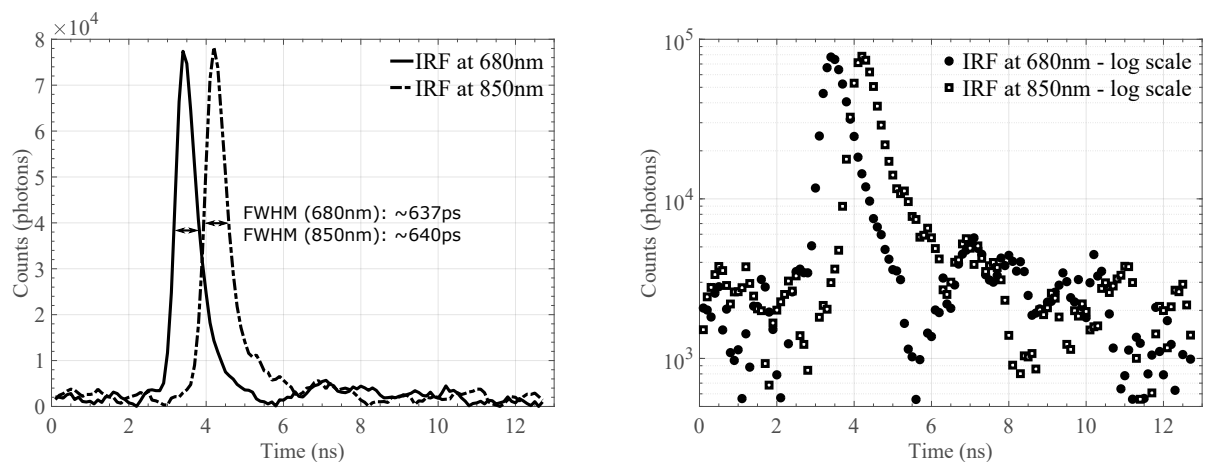


Figure 2. The resulting IRFs for both wavelengths after cross-correlation with the transmitted MLSs in linear-(left) and log-scale (right).

3.1 SYSTEM'S IMPULSE RESPONSE FUNCTIONS

Indicative system's IRFs for both wavelengths in linear- and log-scale can be found in Figure 2. The FWHM has been computed for each wavelength and it has been found to be $\sim 637\text{ps}$ and $\sim 640\text{ps}$ for the 680nm and 850nm source, respectively, demonstrating the satisfactory performance of the custom-made optical transceiver, which is comparable to the commercially available one. Compared to the IRF of the single-channel setup shown in our previous work⁸, the IRF of the 850nm source has increased by $\sim 60\text{ps}$ due to the additional components that have been placed between the sources and the SPCM detectors in the current setup. A log-scale representation of both IRFs reveals that for both wavelengths the dynamic range is almost the same and equals approximately two orders of magnitude. Our system's dynamic range is roughly one or two orders of magnitude lower than other reported traditional TD NIRS instruments^{1,11}. It is also worth noting that our IRFs' floor is much noisier compared to traditional pulse excitation-based IRFs, a trade-off stemming from the spread spectrum approach, which spreads the system's noise across the whole frequency spectrum uniformly, thus, deviating from the Poisson noise of conventional TD NIRS systems⁸.

3.2 STABILITY

The stability of the two sources has been investigated over an eight hour period. During this time, the intensity and relative mean ToF variations of the VCSELs were recorded every 5 minutes. The collective results for both wavelengths can be found in Figure 3, where the top two Figures demonstrate the intensity and relative mean ToF for the 680nm VCSEL, while the bottom two Figures refer to the 850nm source.

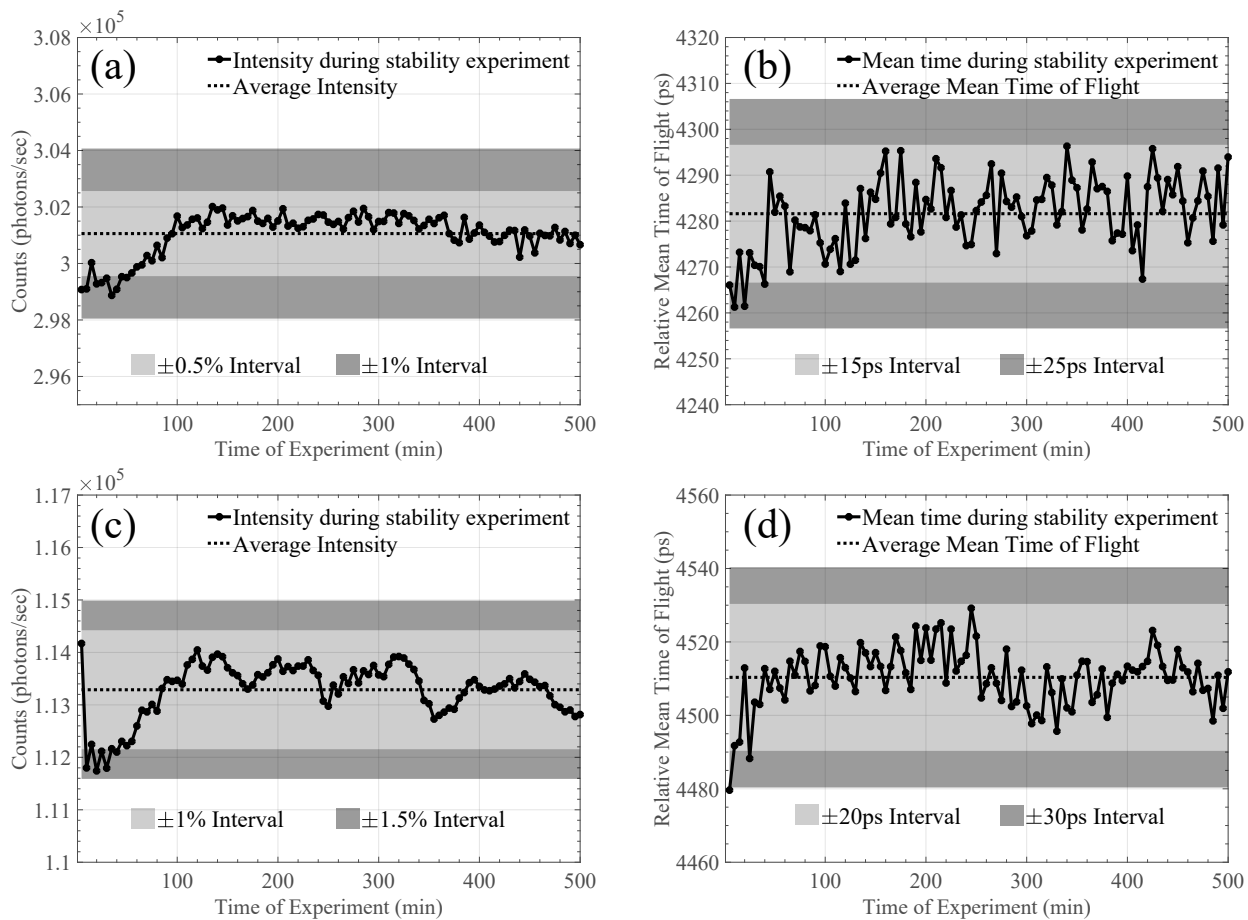


Figure 3. Stability experiment for (a) the intensity and (b) the photon relative mean TOF of the 680nm VCSEL using the proposed system over eight hours. Similarly, in (c) and (d) for the 850nm VCSEL source.

Following an initial *warm-up* period of ~ 35 -40 minutes, the intensity variations of the 680nm source are $\pm 0.5\%$, while the recorded relative mean ToF demonstrates stability of ± 15 ps. The 850nm source is behaving in a similar manner, illustrating $\pm 1\%$ and ± 20 ps variations in intensity and relative mean ToF, after the same *warm-up* period. Once again, it is worth stressing the fact that within the first ~ 35 -40 minutes our sources have managed to achieve the aforementioned intensity and relative mean ToF stability, a time period significantly lower compared to some pulsed conventional instruments that typically need more than a few hours to reach similar intensity and mean TOF stability values^{1, 12-14}.

3.3 LINEARITY AND ACCURACY

In our previous work⁸ the linearity and accuracy of the 850nm source has been shown and thoroughly discussed. Here we present linearity and accuracy results for the new, custom-made 680nm source, using the exact same experimental protocol and liquid-based phantoms, in which suitable absorbing and scattering agents were added to deionised water to control the absorption and reduced scattering coefficients (μ_a and μ'_s respectively) of the final solution⁸. The same near-infrared absorbing dye S109564 (ICI, U.K.) has been selected to adjust the absorption coefficient and 20% W/V intralipid (Fresenius Kabi, U.K.) has been used again to modify the reduced scattering coefficient. Both substances were thoroughly characterised as shown here⁸. The results of these linearity and accuracy experiments are presented in Figure 4.

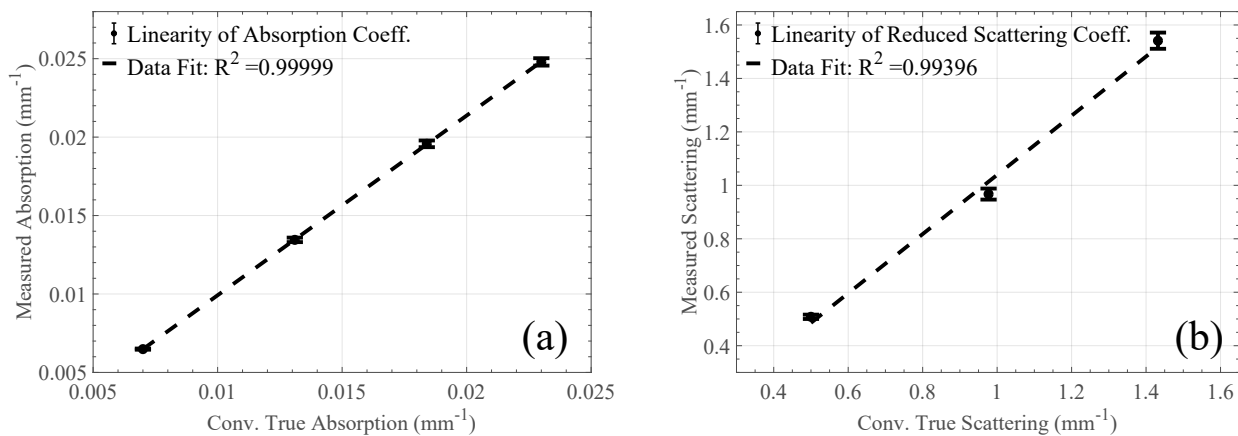


Figure 4. Linearity for the (a) absorption and (b) reduced scattering coefficients of the 680nm source. The error bars demonstrate the standard deviation between repeated measurements (10 for each point) and the dashed lines represent the first order linear fit of their mean values.

Again, two sets of experiments were conducted. The linearity of the recovered absorption coefficient was determined by holding the scattering coefficient almost constant at $\mu'_s = 0.8\text{mm}^{-1}$, whilst the absorption coefficient was varied over the range $0.007 \leq \mu_a \leq 0.023\text{mm}^{-1}$. On the other hand, when the linearity for reduced scattering coefficients was measured, μ_a value was held almost constant and set equal to 0.01mm^{-1} , while μ'_s was increased to achieve nominal values of 0.5, 0.977 and 1.432mm^{-1} . Again, ten measurements on each phantom were taken and the obtained TPSFs were subsequently fitted to the previous standard model of photon diffusion theory¹⁵ by using the same nonlinear least-squares fit algorithm in Matlab[®]. All ideal TPSFs produced by the theoretical model were convolved with our system's IRF before proceeding with the actual fitting algorithm. Once again, the results summarised in Figure 4a and Figure 4b demonstrate the linearity of the system, whose coefficient of determination for both experiments is greater than 0.99. The relative accuracy error for each experiment ranged between 3 and 8% for the absorption coefficient experiment and between 1 and 7% for the scattering one.

4. IN VIVO EXPERIMENTAL VALIDATION

The ultimate purpose of the implemented instrument is the reliable monitoring of various haemodynamic responses of the human body. Cuff occlusion of the upper left arm (220mmHg) has been selected on an adult male as a quick, proof-of-concept test that would allow us to assess the capabilities of our system. The same protocol

that was shown in our previous work⁸ has been followed and is described again here for the reader's convenience. The experiment consists of three stages: In the first one the arm was in a resting position for 120 seconds; then the cuff was rapidly inflated to a pressure of 220mmHg to provide an abrupt vascular (venous and arterial) occlusion, maintained for another 120 seconds; and finally the cuff was released and the recovery phase followed for 120 more seconds. The only experimental difference between our previous and current attempt was the separation between the source and detectors fibres, which this time were placed on the subject's forearm 20mm apart. The fibres were stabilised on the forearm using a flexible 3D-printed base (TangoBlack⁺ material printed by a Stratasys Objet Connex 500 3D printer) with acrylic ferrules on top of it for additional fibre stabilisation. As a precaution, bandages have been also added around the 3D-printed base to ensure the fixed position between the source and detector fibres. The experiment was performed in dark room conditions and the integration time for each TPSF was set equal to 0.2 seconds. For the experimental result shown below, 25 TPSFs were averaged for each data point, resulting into an integration time of 5 seconds. The recorded haemodynamic responses can be seen in Figure 5.

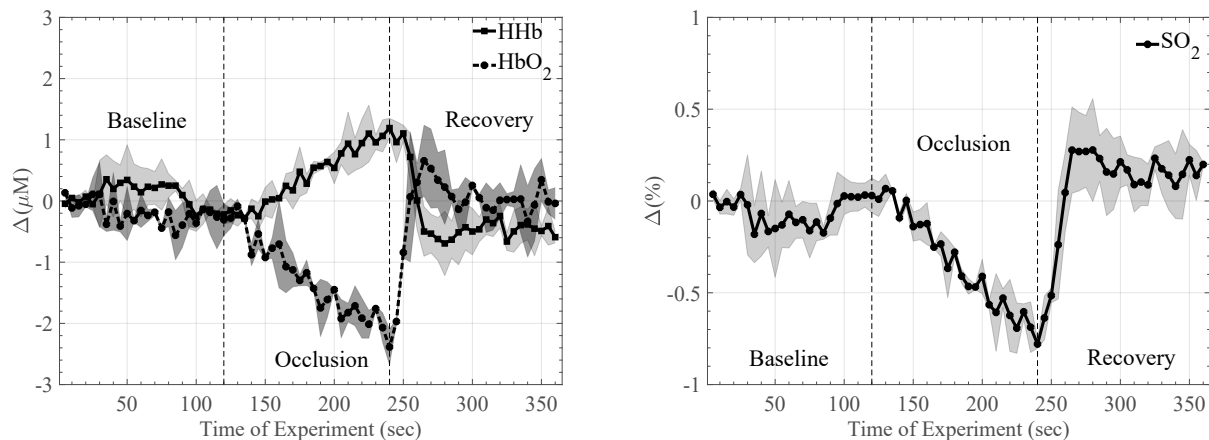


Figure 5. Left upper arm venous-arterial cuff occlusion validation for 2 consecutive measurements on the same subject. The changes of the haemodynamic parameters have been plotted with respect to the baseline, defined as the beginning of the experiment. The dashed lines mark the three distinct periods of the experiment.

The left plot in Figure 5 demonstrates the almost complementary changes between HHb and HbO₂, while the right plot shows the time response of SO₂, calculated as $[SO_2] = [HbO_2] / ([HbO_2] + [HHb])$ ^{9,16}. The concentration values of HHb and HbO₂ have been computed using the modified Beer-Lambert law, based on the measured intensity and mean ToF changes for both wavelengths during the experiment, provided by our instrument. The differential pathlength factor (DPF) has been determined via measurement of the mean time taken for light to traverse the scattering medium, as explained in detail in the literature^{16,17}. During the arterial occlusion period (here between 120 and 240 seconds), oxygenated blood cannot access the occluded blood, however, muscle continues the oxygen consumption. Therefore there is a steady decrease in HbO₂ and since the muscle metabolism has not changed during this period there is also an increase in HHb. This results in an overall decrease in SO₂, which reflects the tissue's oxygenation condition. After the occlusion period, the cuff was released fast and consequently a hyperaemia peak is observed in all reported haemodynamic parameters. However, all parameters tend to return to the initial baseline. The experiment was performed twice on the same subject sequentially and the results in Figure 5 demonstrate the mean and standard deviation values of these two measurements. The instrument is capable of providing distinct haemodynamic parameters changes with integration times even down to 1 second, however, this inevitably has an impact upon the standard deviation of the measurements.

5. CONCLUSIONS

Herein, a dual-wavelength TD NIRS instrument has been demonstrated, relying entirely upon the spread spectrum technique. This work has been the natural progression of our previous single-channel spread spectrum TD NIRS system and, to the best of our knowledge, this is the first time in literature that a multi-channel

spread spectrum system has been used for *in vivo* spectroscopic measurements. The system's IRFs as well as its stability, linearity and accuracy are comparable to those of traditional TD instruments, while its cost still remains significantly lower, with each VCSEL source costing no more than £60 in total. The size of both optical transceivers is the one of a standard commercial SFP/SFP+ connector.

The encouraging characterisation and *in vivo* results demonstrate the potentials of the instrument and highlight its performance. Future work will focus on the improvement of the current system's performance even further. So far, we were limited by the optical power of the AVAGO Gigabit transceiver, which has a fixed output value. In the future, an upgraded spread spectrum spectroscopic system will feature a custom-made high-speed, high-power 850nm VCSEL-based optical transceiver, which together with the current 680nm transceiver will allow us to control the output power of both VCSELs and achieve even higher count rates. We aspire to use the current system in various fNIRS *in vivo* experiments, in order to evaluate its performance as an alternative, portable, low-cost human brain mapping spectroscopic instrument for various applications.

ACKNOWLEDGMENTS

We acknowledge the financial support of the EPSRC (EP/N032055/1) and the Royal Academy of Engineering (RF1516/15/33). We would also like to sincerely thank Vixar Inc. for kindly providing us with their ultra-high performance VCSELs.

REFERENCES

- [1] Torricelli, A., Contini, D., Pifferi, A., Caffini, M., Re, R., Zucchelli, L., and Spinelli, L., "Time domain functional NIRS imaging for human brain mapping," *Neuroimage* **85**, 28–50 (2014).
- [2] Chitnis, D., Cooper, R. J., Dempsey, L., Powell, S., Quaggia, S., Highton, D., Elwell, C., Hebden, J. C., and Everdell, N. L., "Functional imaging of the human brain using a modular, fibre-less, high-density diffuse optical tomography system," *Biomedical optics express* **7**(10), 4275–4288 (2016).
- [3] Arridge, S. R., "Optical tomography in medical imaging," *Inverse problems* **15**(2), R41 (1999).
- [4] Powell, S., Cooper, R. J., Hebden, J. C., and Arridge, S. R., "Dynamic image reconstruction in time-resolved diffuse optical tomography," in [*Optical Tomography and Spectroscopy of Tissue XI*], **9319**, 93191I, International Society for Optics and Photonics (2015).
- [5] Chen, N. G. and Zhu, Q., "Time-resolved optical measurements with spread spectrum excitation," *Optics letters* **27**(20), 1806–1808 (2002).
- [6] Chen, N. G. and Zhu, Q., "Time-resolved diffusive optical imaging using pseudo-random bit sequences," *Optics express* **11**(25), 3445–3454 (2003).
- [7] Mehta, K., Hasnain, A., Zhou, X., Luo, J., Penney, T. B., and Chen, N., "Spread spectrum time-resolved diffuse optical measurement system for enhanced sensitivity in detecting human brain activity," *Journal of Biomedical Optics* **22**(4), 045005–045005 (2017).
- [8] Papadimitriou, K. I., Dempsey, L. A., Hebden, J. C., Arridge, S. R., and Powell, S., "A spread spectrum approach to time-domain near-infrared diffuse optical imaging using inexpensive optical transceiver modules," *Biomedical Optics Express* **9**(6), 2648–2663 (2018).
- [9] Hillman, E. M., Hebden, J. C., Schmidt, F. E., Arridge, S. R., Schweiger, M., Dehghani, H., and Delpy, D. T., "Calibration techniques and datatype extraction for time-resolved optical tomography," *Review of Scientific Instruments* **71**(9), 3415–3427 (2000).
- [10] Dixon, R. C., [*Spread spectrum systems: with commercial applications*], vol. 994, Wiley New York (1994).
- [11] Cooper, R. J., Magee, E., Everdell, N., Magazov, S., Varela, M., Airantzis, D., Gibson, A. P., and Hebden, J. C., "MONSTIR II: a 32-channel, multispectral, time-resolved optical tomography system for neonatal brain imaging," *Review of Scientific Instruments* **85**(5), 053105 (2014).
- [12] Contini, D., Torricelli, A., Pifferi, A., Spinelli, L., Paglia, F., and Cubeddu, R., "Multi-channel time-resolved system for functional near infrared spectroscopy," *Optics Express* **14**(12), 5418–5432 (2006).
- [13] Re, R., Contini, D., Turola, M., Spinelli, L., Zucchelli, L., Caffini, M., Cubeddu, R., and Torricelli, A., "Multi-channel medical device for time domain functional near infrared spectroscopy based on wavelength space multiplexing," *Biomedical optics express* **4**(10), 2231–2246 (2013).

- [14] Re, R., Pirovano, I., Contini, D., Spinelli, L., and Torricelli, A., “Time domain near infrared spectroscopy device for monitoring muscle oxidative metabolism: Custom probe and in vivo applications,” *Sensors* **18**(1), 264 (2018).
- [15] Arridge, S. R., Cope, M., and Delpy, D., “The theoretical basis for the determination of optical pathlengths in tissue: temporal and frequency analysis,” *Physics in Medicine & Biology* **37**(7), 1531 (1992).
- [16] Hillman, E. M. C., *Experimental and theoretical investigations of near infrared tomographic imaging methods and clinical applications*, PhD thesis, University College London (2002).
- [17] Okada, E., Firbank, M., Schweiger, M., Arridge, S. R., Cope, M., and Delpy, D. T., “Theoretical and experimental investigation of near-infrared light propagation in a model of the adult head,” *Applied optics* **36**(1), 21–31 (1997).